



**Guest Removal from Ring-Banded Guanidinium
Organosulfonate Hydrogen-Bonded Frameworks**

Journal:	<i>Nanoscale</i>
Manuscript ID	NR-ART-01-2025-000467.R1
Article Type:	Paper
Date Submitted by the Author:	06-Apr-2025
Complete List of Authors:	<p>Spencer, Rochelle; New York University, Chemistry Yusov, Anna; New York University, Chemistry Dillon, Alexandra; New York University, Chemistry Tiwari, Akash; New York University, Chemistry Arteaga, Oriol; University of Barcelona, Department of Applied Physics and Optics, IN2UB Sburlati, Sophia; New York University, Chemistry Whittaker, St. John; New York University, Chemistry Wu, Wantong; New York University, Chemistry Chen, Zoey; New York University, Chemistry Shtukenberg, Alexander; New York University, Department of Chemistry Ward, Michael; New York University, Chemistry Kahr, Bart; New York University, Department Chemistry and Molecular Design Institute Lee, Stephanie; New York University, Chemistry</p>

ARTICLE

Guest Removal from Ring-Banded Guanidinium Organosulfonate Hydrogen-Bonded Frameworks†

Received 00th January 20xx,
Accepted 00th January 20xx

DOI: 10.1039/x0xx00000x

Rochelle B. Spencer,^a Anna Yusov,^a Alexandra M. Dillon,^a Akash Tiwari,^a Oriol Arteaga,^b Sophia Sburlati,^a St. John Whittaker,^a Wantong Wu,^a Zoey Chen,^a Alexander G. Shtukenberg,^a Michael D. Ward,^{*a} Bart Kahr^{*a} and Stephanie S. Lee^{*a}

Crystalline fibers of the hydrogen-bonded framework bis(guanidinium) naphthalene-1,5-disulfonate, (G)₂(1,5-NDS), with ethanol guest molecules twist as they grow when deposited from solution under conditions that favor low nucleation densities and high branching rates. Spherulites comprising helicoidal fibers with a pitch of $3.4 \pm 0.5 \mu\text{m}$ display rhythmic concentric variations in interference colors between crossed polarizers. Tightly packed fibers and platelets, systematically change orientations between flat-on and edge-on crystallites with respect to the substrate surface. Mueller matrix imaging reveals periodic oscillations in the absolute magnitude of the linear retardance and an associated bisignate circular retardance. Single-crystal X-ray diffraction data demonstrates that the twisted (G)₂(1,5-NDS) ⊃ EtOH crystals adopt a bilayer packing motif with ethanol as guest molecules (space group $P\bar{1}$). When the banded spherulite films were subsequently heated at 130°C, the solvated phase was converted to a guest-free crystalline phase (space group $P2_1/c$). This transition resulted in loss of linear retardance.

Introduction

During the past three decades, more than 700 hydrogen-bonded framework crystal structures constructed from guanidinium (G) cations and organosulfonate (S) anions have been reported.^{1–7} Meanwhile, our laboratory has established that more than 1/3 of molecular crystals can be made to twist as they grow under large driving forces.⁸ Herein, the intersection of these two large sets of materials is explored. Twisted crystals, besides presenting puzzles for crystal characterization and mechanism, promise applications in optics and electronics that emerge from the regular precession of crystal orientations normal to substrates in thin films.^{9–15} Since GS frameworks can include a wide range of functional guest molecules by design, twisted GS frameworks may provide a pathway to modulate charge and photon transport in twisted crystals.^{16–19}

Twisted molecular crystals are most frequently grown from the melt at large undercoolings²⁰ but they also can form from solution^{21–24} or vapor.²⁵ Their crystallization often proceeds through spherulitic growth of helicoidal fibers that twist in

concert about the growth direction, presenting continuously rotating crystal orientations at the film surface. The growth of banded spherulites comprising concentric bands of alternating interference colors between crossed polarizers is attributable to crystal orientation-dependent refractivities. Crystal twisting may also introduce periodic oscillations in all $\langle hkl \rangle$ dependent properties, including absorbance,^{10, 12} electrical conductivity,^{9, 10, 12} fluorescence,^{10, 12} reactivity,¹⁵ and solubility.²⁶

Twisting imparts chirality on the mesoscale to crystalline films. Banded spherulites of centrosymmetric compounds generally form helicoidal fibers that twist clockwise about the growth directions in some regions and counterclockwise elsewhere. The resulting sensitivity to circularly polarized light is not natural optical activity²⁷ of homogeneous media but arises from the splay sense of overlaid crystalline lamellae along the direction of light propagation.²⁸ The films are not optically homogeneous, neither in the plane of the film (xy) nor along the wave vector (z).

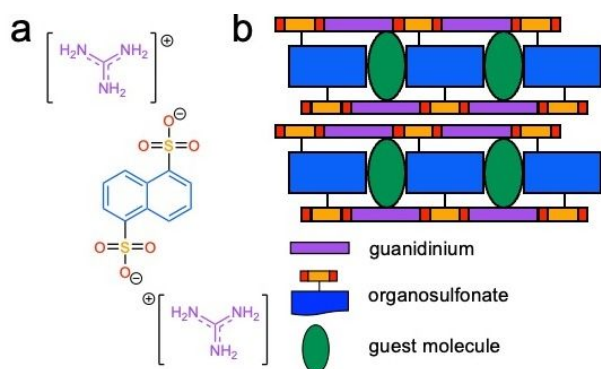
We report herein twisted crystal films of a bis(guanidinium) naphthalene-1,5-disulfonate framework containing ethanol guest molecules, denoted herein as (G)₂(1,5-NDS) ⊃ EtOH, by solution processing. Scheme 1a depicts schematically the solid-state architecture of (G)₂(1,5-NDS) ⊃ EtOH. The naphthalene groups appended to the sulfonates serve as pillars that connect opposing GS sheets to form bilayers that stack in the third dimension (Scheme 1b). The pillars enforce inclusion cavities in the gallery regions between adjacent GS sheets that can accommodate guest molecules, such as ethanol (green ovals in Scheme 1b). (G)₂(1,5-NDS) ⊃ EtOH crystals adopt $P\bar{1}$ symmetry, confirmed by single-crystal X-ray diffraction analysis. Distinct

^a New York University, Molecular Design Institute, Department of Chemistry, New York, NY 10003, USA.

^b University of Barcelona, Department of Applied Physics, 08028 Barcelona, Spain.

*mdw3@nyu.edu, bk66@nyu.edu, stephlee@nyu.edu

† Electronic Supplementary Information (ESI) available: Optical micrographs between crossed polarizers of (G)₂(1,5-NDS) films grown from ethanol at various temperatures and concentrations, PXRD and Mueller matrix micrographs of (G)₂(1,5-NDS) ⊃ EtOH films before and after ethanol removal, absorption and emission spectra of (G)₂(1,5-NDS) in ethanol, visualization of bilayer distances, hydrogen bonds, and void spaces in (G)₂(1,5-NDS) ⊃ EtOH and (G)₂(1,5-NDS). See DOI: 10.1039/x0xx00000x



Scheme 1. (a) Composition of bis(guanidinium) naphthalene-1,5-disulfonate, $(G)_2(1,5-NDS)$. (b) Bilayer architecture formed by $(G)_2(1,5-NDS)$ host-guest framework, highlighting guanidinium cations (purple), naphthalene pillars (blue), sulfonate anions (yellow and red) and guest molecules (green).

left- and right-handed domains observed in Mueller matrix micrographs of thin films of this compound reveal the presence of symmetry breaking mesostructures in banded spherulites. Guest removal upon heating affords nucleation and growth of guest-free $(G)_2(1,5-NDS)$ crystals with $P2_1/c$ symmetry. This transformation is accompanied by a loss of linear retardance in the films.

Results and discussion

Solution deposition of $(G)_2(1,5-NDS) \supset EtOH$ films

$(G)_2(1,5-NDS) \supset EtOH$ films were prepared by heating solutions of 0.10, 0.25, 0.50, 1.0, 2.0, 5.0 and 10 mg/mL $(G)_2(1,5-NDS)$ in ethanol at 50°C, followed by drop casting 30 μ L of solution onto pre-cleaned glass coverslips at -78, 0, 25, 40, 50 and 60°C. The temperature was held constant until solvent evaporation was complete, typically within 1 minute at 60°C to 1 hour at -78°C. Optical micrographs of the films between crossed polarizers were obtained (Figure S1).

At low solute concentrations ranging from 0.25 - 1.0 mg/mL, three distinct crystal morphologies were observed as a function of deposition temperature (Figure S1). High temperatures (40 - 50°C) drove rapid solvent evaporation, resulting in the formation of "coffee" rings of small crystalline aggregates. These rings appeared due to periodic droplet pinning at the solution/air substrate interface. Marangoni flow transports solute molecules to the pinned interface, locally increasing the solute concentration high above the solubility limit and inducing rapid crystal nucleation.²⁹⁻³¹ At intermediate deposition temperatures between 0 - 25°C, $(G)_2(1,5-NDS) \supset EtOH$ crystals grew as spherulites. In this regime, the solvent evaporation rate is slower, resulting in lower supersaturation compared to those at higher deposition temperatures. A combination of lower nucleation rates and strong crystal branching results in spherulitic growth.^{32, 33} Decreasing the temperature further to -78°C to suppress crystal branching while maintaining low nucleation rates resulted in the growth of needle-like crystals

with average lengths of $50 \pm 20 \mu\text{m}$. At the highest concentration of 10 mg/mL, crystalline aggregates were observed across all deposition temperatures. At this concentration, high supersaturation was achieved early in the film drying process for all temperatures, resulting in nucleation within the droplet, not only at the interfaces. A summary of crystal morphologies as a function of concentration and temperature is provided in Figure S2.

Surprisingly, spherulites with concentric alternating bright and dark bands between crossed polarizers emanating from the spherulite center were observed in the spherulitic growth regime at intermediate and high concentrations, indicated by red points in Figure S2. The distance between bright bands was $3.4 \pm 0.5 \mu\text{m}$ across all concentrations and temperatures (Figure S1). Banded spherulite growth in molecular crystals is most frequently observed during rapid crystallization from the melt in which large crystallization driving forces promote the growth of long, thin crystal fibers that spontaneously twist.⁸ Banded spherulites also have been observed, albeit less frequently, in the solution-phase crystallization of organic molecules,^{23, 24} inorganic salts,³⁴ and polymers.³⁵ The interference pattern of these banded spherulites displayed in Figure 1a can be a telltale sign of crystals twisting as they grow radially outwards from the nucleus.³⁶ Alternatively, similar micrographs can be obtained from solutions that crystallize rhythmically.

Banded spherulite microstructure

Rhythmic deposition and coherent polycrystalline helical twists both appear as banded spherulites and are not always obviously differentiated. Moreover, rhythmic precipitation and helicoidal twisting can be coincident.³⁷ Rhythmic precipitation is more common in multicomponent solutions as compared with unimolecular melts, although the dichotomy is not sharp.

Top-view scanning electron micrographs (SEMs) of a $(G)_2(1,5-NDS) \supset EtOH$ banded spherulite at different magnifications are displayed in Figures 1b and c with the spherulite center denoted by a dashed black circle in Figure 1b. Alternating concentric dark bands with smooth surfaces and bright bands with rough surfaces, false-colored blue and yellow, respectively in Figure 1c are discernible. The spacing between these two types of surfaces is commensurate with the band spacing measured in the optical micrograph between crossed polarizers in Figure 1a. Upon closer examination, the SEMs reveal a homogenous film with an accordion-like topology. Some well-formed, continuous helices are observed. Some crystals twist by as much as 180° after which, radial growth is carried forward by new fibers from new nuclei.

Although rhythmic variations in fiber density are observed, there is no direct evidence for rhythmic growth. The density of the deposited material changes rhythmically, producing thick and thin sub-bands that dominate the film topography as revealed in Figure 1c, not unlike the topology of potassium dichromate crystals grown from aqueous media in which banded spherulites deposit rhythmically and afford twisted component crystals.³⁴ Fiber thicknesses in dark and bright

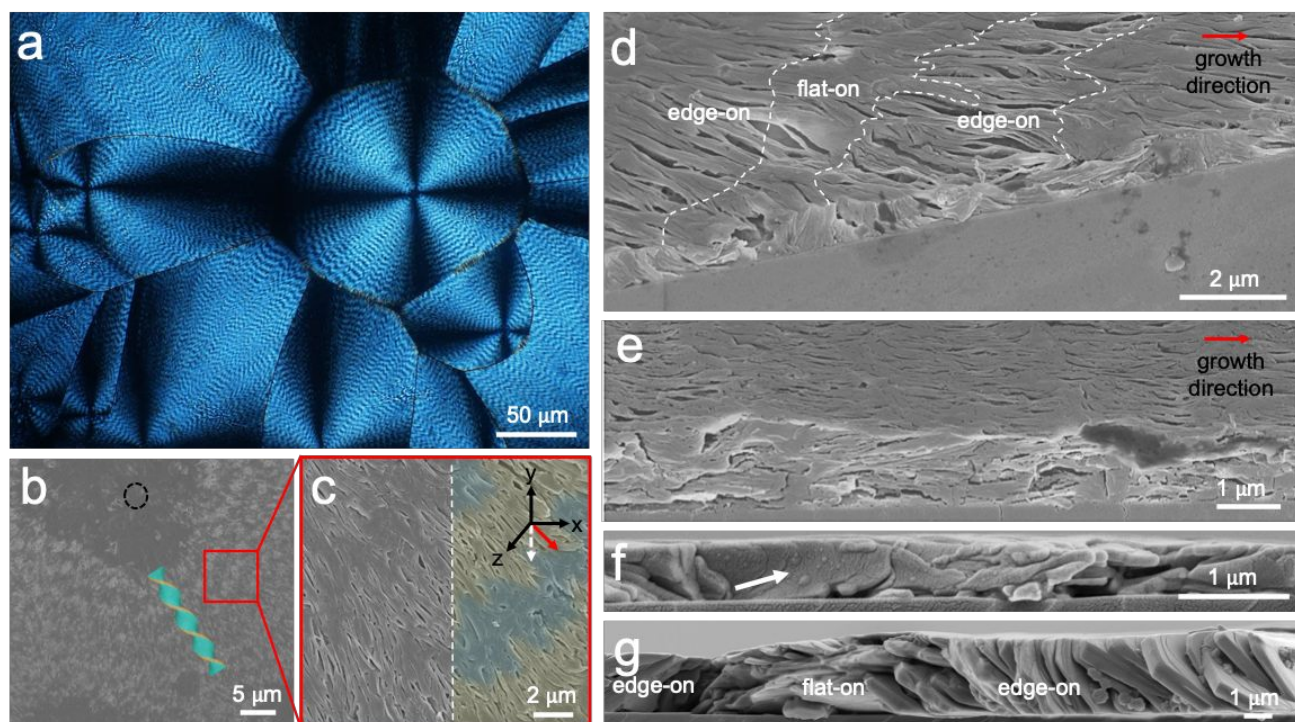


Figure 1. (a) Optical micrograph of a $(G)_2(1,5\text{-NDS})\supset\text{EtOH}$ film viewed between crossed polarizers. (b) Top-view scanning electron micrograph (SEM) of a $(G)_2(1,5\text{-NDS})\supset\text{EtOH}$ film. The spherulite center is highlighted by a dashed black circle. A schematic of a single twisted fiber is overlaid to highlight flat-on and edge-on oriented bands in blue and yellow, respectively. (c) Magnified region of the top-view SEM image with the white solid arrow on the axes showing where the banded spherulite film was cut along a 45° angle relative to the spherulite growth direction (red arrow on axes). (d) Partial SEM top-view and cross-section of a $(G)_2(1,5\text{-NDS})\supset\text{EtOH}$ film collected at a 45° angle relative to the spherulite growth direction and (e) parallel to the spherulite growth direction using a 45° SEM mount. (f) SEM cross-section of a $(G)_2(1,5\text{-NDS})\supset\text{EtOH}$ film collected parallel to the spherulite growth direction and (g) at the terminus of a banded spherulite using a 90° SEM mount. The white arrow in (f) emphasizes curvature in crystallites in the film cross-section.

bands were 330 ± 80 nm and 160 ± 20 nm, respectively. These crystal dimensions are consistent with similar observations of helicoidal fibers of molecular compounds generally adopting a plate-like morphology with one wide and one narrow face along the growth direction.^{10, 26, 27} The orientations for which the wide and narrow faces are parallel and perpendicular to the substrate are referred to here as flat-on and edge-on, respectively. The fibers alternately present their wide and narrow faces in the smooth dark bands and rough bright bands, respectively, as they twist about the spherulite growth direction.

A $(G)_2(1,5\text{-NDS})\supset\text{EtOH}$ banded spherulite film was cut along a 45° angle relative to the spherulite growth direction (illustrated by the white dashed line and solid red arrow, respectively, in Figure 1c) and the cross-section was imaged (Figure 1d - g). Both edge-on and flat-on orientations were visible in the cross-section, with an average film thickness of 1.5 ± 0.5 μm across both bands. Like phthalic acid crystals grown in ethanol-water solution, the growth of $(G)_2(1,5\text{-NDS})\supset\text{EtOH}$ crystals is sometimes discontinuous at the growth front but not entirely discrete.^{23, 38} In some regions of the film in Figure 1d, needles grow, curve, bend, and then terminate repeatedly. New needles nucleate thereafter and stack atop or below quiescent needles. Branching of the crystal plates results in an incoherent

banding pattern that grows with the number of bands, consistent with previous expectations.³⁹

Voids are exposed more frequently between the thin fibers of bright bands compared to the thick fibers of dark bands (Figure 1d, e). Dark bands are filled with wider lamellae that are oriented flat-on, point in the radial direction, and are compact with almost no voids between fibers. Bright bands mainly are a continuation of dark bands and are composed of lamellae that curve or precess about the radial direction to form more compact regions with more crevices between fibers that expose the thin edges of crystals.

SEM images also revealed pronounced curvatures in the film cross-section (white arrow in Figure 1f). Combined with the SEM in Figure 1g, Figure 1f provides evidence that $(G)_2(1,5\text{-NDS})\supset\text{EtOH}$ crystals transition from parallel to perpendicular orientations with respect to the substrate over a distance of ~ 3 μm , commensurate with the band spacing in Figure 1a. Crystal facets are pronounced in Figure 1g because the film was cut just beyond the region where crystal fibers terminated at a grain boundary. The difference in film thickness between Figures 1d-f and 1g arises because the SEM cross-sections were obtained near the edge and center of the spherulite, respectively. Moreover, these images are consistent with crystals that are aligned collectively along the radial direction as they curve,

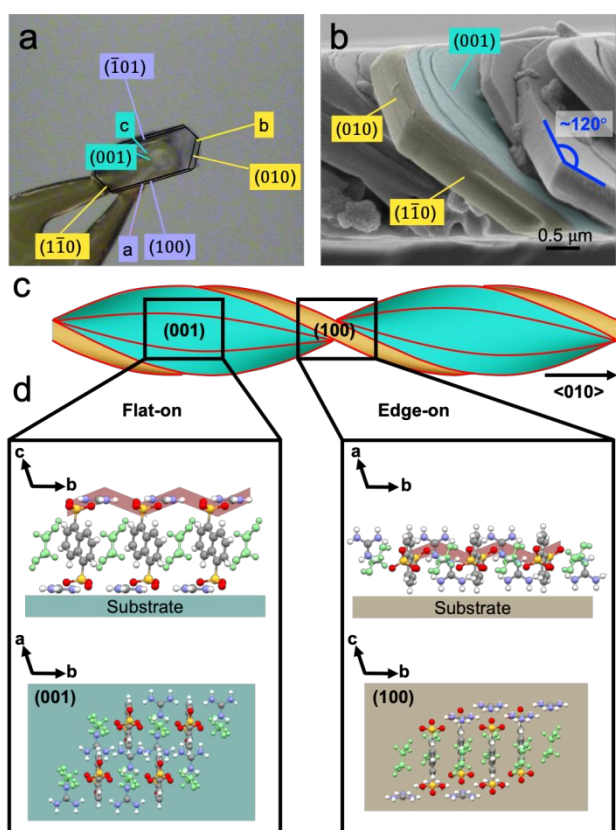


Figure 2. (a) A $(G)_2(1,5\text{-NDS})\supset\text{EtOH}$ indexed single crystal highlighting the (100), (010), (001), $(\bar{1}01)$ and $(\bar{1}\bar{1}0)$ planes, with lattice constants $a = 7.294 \text{ \AA}$, $b = 7.298 \text{ \AA}$, $c = 11.596 \text{ \AA}$, and inter-axial angles $\alpha = 100^\circ$, $\beta = 95^\circ$, $\gamma = 119^\circ$. (b) Cross-sectional SEM image of $(G)_2(1,5\text{-NDS})\supset\text{EtOH}$ banded spherulite film collected at approximately 45° relative to the banded spherulite growth direction, highlighting the (010), (001) and $(\bar{1}\bar{1}0)$ planes, and the facets at the tips of crystals along the growth direction adopting an angle of $\sim 120^\circ$. (c) Schematic illustration of a $(G)_2(1,5\text{-NDS})\supset\text{EtOH}$ helicoidal fiber, highlighting the (001) and (100) planes and the $\langle 010 \rangle$ direction. (d) $(G)_2(1,5\text{-NDS})\supset\text{EtOH}$ crystal orientation relative to the substrate surface and selected planes in flat-on and edge-on oriented crystallites. Major GS ribbons are highlighted in red. Ethanol molecules are shown in green.

bend and progress in the film. Crystals tilt stepwise from left to right in the cross-section whilst decreasing their angular position relative to the substrate. Facets of crystallites with non-zero Gaussian curvature in the SEMs assemble as stacks of crystals much like those produced by solvent-evaporation of pyrene-polyvinylpyrrolidone from dimethylsulfoxide.³⁵

$(G)_2(1,5\text{-NDS})\supset\text{EtOH}$ crystal structure

Distinct facets are clearly visible in some crystals and resemble that of single crystals in Figure 2a, suggesting an associated change in crystallographic orientation as the bands alternate. The powder X-ray diffraction (PXRD) patterns of the twisted $(G)_2(1,5\text{-NDS})\supset\text{EtOH}$ film (Figure S3) did not match any powder

patterns expected from published crystal structures of this GS host. Recrystallization of the $(G)_2(1,5\text{-NDS})$ host framework from ethanol afforded a PXRD pattern for the bulk powder that matched the PXRD pattern of the twisted $(G)_2(1,5\text{-NDS})\supset\text{EtOH}$ film (Figure S3). A single crystal plate of $(G)_2(1,5\text{-NDS})\supset\text{EtOH}$ grown for 7 days from ethanol was indexed (Figure 2a) and its crystal structure was solved in the $P\bar{1}$ space group (Table S1, CSD deposition code: 2419508). The crystal structure of the ethanol solvate revealed the well-documented two-dimensional hydrogen-bonded sheets of G and S ions, wherein the sheets were connected by naphthalene pillars in a bilayer architecture with ethanol guest molecules inside the host cavities.^{7, 40-42} A short distance of 2.988 \AA between oxygen atoms of the ethanol guest and organosulfonate pillar is consistent with hydrogen bonding. Of the 27 reported $(G)_2(1,5\text{-NDS})$ inclusion compounds,^{18, 43-45} only two – $(G)_2(1,5\text{-NDS})\supset\text{benzonitrile}$ and $(G)_2(1,5\text{-NDS})\supset\text{aniline}$ – adopt a bilayer architecture. Others adopt a brickwork architecture. Many bilayer frameworks based on naphthalene-1,5-disulfonate anions have also been reported, albeit the coordinated cation species vary widely.^{46, 47}

Upon closer examination of the film cross-section, distinct facets were clearly visible in some crystals, with the facets at the tips of crystals along the growth direction adopting an angle of $\sim 120^\circ$ (Figure 2b). Comparing the single crystal morphology of crystal plates to that observed in banded spherulite films, the (001) and (100) planes were assigned to the wide and narrow faces of the helicoidal fibers, respectively. The long axis of the fibers was likewise corresponded to $\langle 010 \rangle$.

A combination of crystal shape and SCXRD analysis provides the morphology of a helicoidal $(G)_2(1,5\text{-NDS})\supset\text{EtOH}$ fiber as it twists about $\langle 010 \rangle$ (Figure 2c). Flat-on orientations present the (001) face parallel to the substrate, corresponding to the quasi-hexagonal hydrogen-bonded sheets of G cations and S anions. The sheet can be described as containing repetitive hydrogen bonds between N-H groups of G cations and sulfonate O atoms of S anions along major and minor “ribbons” that coincide with the b and c axes, respectively.⁴⁸ Edge-on orientations, on the other hand, present the (100) plane parallel to the substrate, exposing the naphthalene pillars between the GS sheets at the edges. Figure 2d displays flat-on and edge-on orientations of crystals relative to the substrate surface from both side and top views. Twisting occurs along the major ribbon (b axis) in $(G)_2(1,5\text{-NDS})\supset\text{EtOH}$ (highlighted in red in Figure 2d).

Polarimetric analysis of banded spherulites

The optical properties of $(G)_2(1,5\text{-NDS})\supset\text{EtOH}$ banded spherulites were mapped using a homebuilt Mueller matrix imaging (MMI) microscope based on a newly commercialized polarization-sensitive camera with silicon grating micro-polarizer arrays etched at orientations of 0° , 45° , 90° and 135° , in front of the quadrants of super-pixels (tetrads of pixels) of a sensor.⁴⁹ The polarization state generator involves a fixed linear polarizer and a wave plate that rotates among predetermined positions.

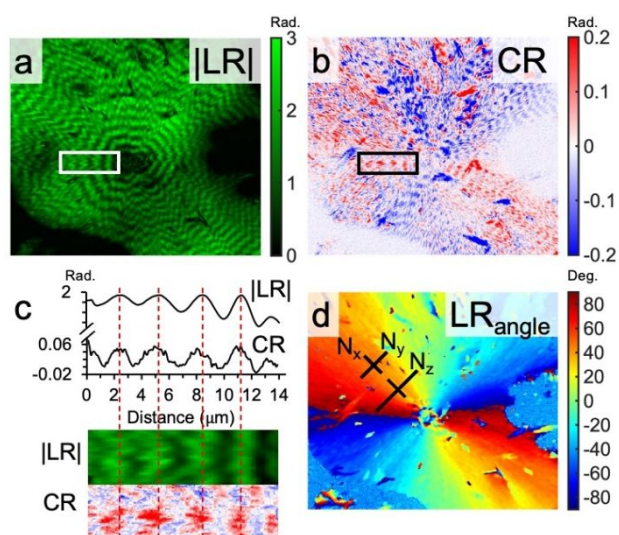


Figure 3. (a) Linear retardance ($|LR|$) map and (b) circular retardance (CR) map of $(G)_2(1,5\text{-NDS})\supset\text{EtOH}$ banded spherulite films. (c) Extracted optical properties along the fiber growth direction indicated by the white and black rectangles in (a) and (b), respectively. Vertical red lines highlight shifts between the $|LR|$ and CR extrema. (d) Angle-dependent linear retardance (LR_{angle}) map measured in degrees counterclockwise from the horizontal direction. The relative magnitudes of the refractive indices perpendicular and parallel to the spherulite growth direction, $N_x < N_y < N_z$, are represented by the black lines in (d). $\lambda = 455$ nm.

The instrument is not a complete polarimeter. It does not deliver the 16 elements of the 4×4 polarization transfer or Mueller matrix. Because linear analyzers cannot detect the ellipticity of the output, the fourth element of the Stokes vector is ill-determined and only the first three rows (12 elements) of the Mueller matrix \mathbf{M} were established. However, it was shown that because three rows are sufficient for generating the corresponding Jones matrix, and the Jones matrix can be expanded to a Mueller matrix for a non-depolarizing sample, the missing row of \mathbf{M} can be restored.⁵⁰ Optical properties were extracted from the differential matrix \mathbf{m} , given by:

$$\mathbf{m}z = -\ln(\mathbf{M}) = \begin{bmatrix} -k & -LE & -LE' & CE \\ -LE & -k & CR & LR' \\ -LE' & -CR & -k & -LR \\ CE & -LR' & LR & -k \end{bmatrix}$$

where k is the isotropic absorption, LE is the linear extinction, LR is the linear retardance, CE is the circular extinction, and CR is the circular retardance. Dichroism and birefringence are the intrinsic values of the extinction and retardance, respectively. LR' and LE' refer to the differences measured for an intermediate reference frame with axes of $\pm 45^\circ$ with respect to the unprimed quantities. The sample thickness is z .

Figure 3a displays the $|LR|$ signal of a $(G)_2(1,5\text{-NDS})\supset\text{EtOH}$ banded spherulite film collected at $\lambda = 455$ nm, which is outside the absorption band of $(G)_2(1,5\text{-NDS})\supset\text{EtOH}$ (Figure S4). The

$|LR|$ signal oscillates between 0.3 and 1.8 radians along the spherulitic growth direction, a consequence of the continuous rotation of out-of-plane crystallographic orientations. This $|LR|$ map is consistent with the alternating interference bands of the spherulites when viewed between crossed polarizers (Figure 1a), where flat-on oriented dark bands and edge-on oriented bright bands have low and high linear retardance, respectively.

Figure 3b displays a CR map of the same banded spherulite. The CR is expected to be zero for centrosymmetric $(G)_2(1,5\text{-NDS})\supset\text{EtOH}$ crystals. Nevertheless, distinct dextrorotatory (blue) and levorotatory (red) domains are visible in the CR map. Along the spherulite radius, CR oscillates smoothly from almost zero to positive (Figure 3c), in phase with $|LR|$. This optical activity is not natural but arises from the directional splay of crystallites as they twist in concert about the growth direction.⁵¹ The sign of the CR signal depends on the twist sense of the crystals, either clockwise or counterclockwise, which is determined during crystal nucleation. Spatial constraints affect the in-phase twisting of densely packed lamellae.³⁶ Lamellae positioned in the edge-on orientation rotate around the central axes as they twist, increasing their projected length along the x -axis. This leads to potential collisions, which are avoided through spatial repositioning, with the most efficient route being perpendicular to the side surfaces of the lamellae. Divergence of lamellae, splay, establishes the misorientation angle between lamellae such that within a domain of a single twist sense, the CR signal oscillates between 0 and 0.07 radians.

The absorption maxima in solution for $(G)_2(1,5\text{-NDS})\supset\text{EtOH}$ lie between 200 nm and 315 nm in the UV region (Figure S4). The Mueller matrix imaging microscope is equipped with glass optics and therefore limited to measurements in the visible range. There is no evidence of CE or LE at 455 nm.

The generation of optical activity by twisting $(G)_2(1,5\text{-NDS})\supset\text{EtOH}$ crystals occurs spontaneously during crystallization from solution. Twisted molecular crystals of other compounds such as potassium dichromate and phthalic acid exhibit similar morphologies and in some cases evidence of optical activity.³⁸ Thin lamellae that comprise banded spherulites splay as they twist in concert due to space constraints. The resulting misorientation of these stacked lamellae produces a CR signal.³⁶

Figure 3d displays the LR_{angle} map of the banded spherulite. LR_{angle} is the orientation of the slow vibration direction (the largest refractive index) measured counterclockwise from the horizontal axis. Crystals are oriented radially albeit the direction with the highest refractive index is consistently tangential as the crystals twist, indicating that the smallest refractive index lies along the growth direction. The spherulite is optically positive with relative refractive indices $N_x < N_y < N_z$, where N_y and N_z correspond to the dark and bright bands of the banded spherulite, respectively (black lines in Figure 3d).

Guest removal from $(G)_2(1,5\text{-NDS})\supset\text{EtOH}$ single crystals

Generating optical activity from the splayed stacking of linearly birefringent crystals (as opposed to natural optical activity arising from molecular chirality) provides an opportunity to tune the optical activity through crystal transformations. To

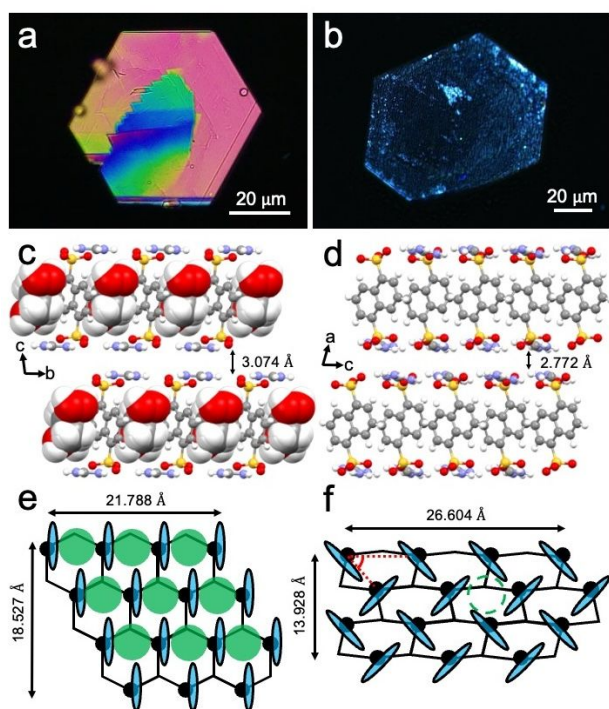


Figure 4. (a, b) Optical micrographs of a $(G)_2(1,5\text{-NDS})\text{EtOH}$ single crystal between crossed polarizers before and after ethanol removal at 130°C overnight. (c, d) Crystal structures of $(G)_2(1,5\text{-NDS})\text{EtOH}$ and guest-free $(G)_2(1,5\text{-NDS})$ depicted as ball-and-stick with disordered ethanol guest molecules as space-filling. The $(G)_2(1,5\text{-NDS})$ single crystal has lattice constants $a = 11.359 \text{ \AA}$, $b = 9.285 \text{ \AA}$, $c = 9.048 \text{ \AA}$, and inter-axial angles $\alpha = 90^\circ$, $\beta = 101^\circ$, $\gamma = 90^\circ$. The distance between adjacent bilayers is 3.074 \AA and 2.772 \AA , respectively. (e, f) Projection topologies for GS sheets observed in $(G)_2(1,5\text{-NDS})\text{EtOH}$ and $(G)_2(1,5\text{-NDS})$ crystal structures. Black filled circles depict S anions. G cations sit on the undecorated nodes of the hexagonal tiling. Blue discs depict naphthalene pillars. The green filled circles in (e) show ethanol guest molecules. The green dashed circle in (f) depict voids in the framework. The angle between naphthalene pillars in $(G)_2(1,5\text{-NDS})$ is 87.71°.

date, single crystal-to-single crystal transformations have been observed in several GS frameworks through guest exchange^{52, 53} and desolvation.^{54, 55} Such transformations are accompanied by changes in optical properties as a result of differences in polarizabilities and absorptivities of guest molecules, as well as molecular rearrangement in the framework itself.

Single crystals of $(G)_2(1,5\text{-NDS})\text{EtOH}$ were heated at 130°C overnight to determine if ethanol guest molecules could be released from the framework without loss of crystallinity. Video S1 displays a $(G)_2(1,5\text{-NDS})\text{EtOH}$ platelike crystal during heating, in which a hexagonal single crystal undergoes a gradual non-cooperative darkening that is fastest along the b axis as ethanol bubbles from the crystal face. Optical micrographs of two different single crystals viewed between crossed polarizers before and after heating are displayed in Figures 4a and 4b, respectively. The solvate crystal in Figure 4a is a highly

birefringent plate that exhibits bright interference colors. After heating, crystals remain highly transmissive but lose their interference colors, as observed in Figure 4b.

SCXRD analysis of a single crystal of $(G)_2(1,5\text{-NDS})\text{EtOH}$ that was heated at 130°C revealed a crystal structure consistent with removal of ethanol from the framework. Thin crystals exhibited greater orientation, fewer domains and transparency upon guest removal (indicated by white arrows in the optical micrographs of Figure S5), whereas thicker, guest-free crystals displayed more domains, reduced orientation and an opaque appearance (indicated by red arrows in the optical micrographs of Figure S5). The guest-free framework, hereafter denoted as $(G)_2(1,5\text{-NDS})$, retained the bilayer architecture with $P2_1/c$ symmetry. Due to the low quality of $(G)_2(1,5\text{-NDS})$ single crystals, only preliminary crystallographic data was collected (see Table S1, Figure S6 and CIF for crystallographic data).

To the best of our knowledge, $(G)_2(1,5\text{-NDS})$ is the first $(G)_2(1,5\text{-NDS})$ framework confirmed as guest-free by SCXRD. A crystal structure of $(G)_2(1,5\text{-NDS})$ with undefined guest molecules, denoted as HOF-GS-10 (CSD deposition code: IWOYAW), was reported in 2016.⁵⁶ The PXRD pattern of $(G)_2(1,5\text{-NDS})\text{EtOH}$ is not substantially different from that reported for HOF-GS-10, although HOF-GS-10 was crystallized from a methanol/acetone mixture (Figure S7). Distinct peaks emerge upon ethanol removal from $(G)_2(1,5\text{-NDS})\text{EtOH}$, notably the peaks around $2\theta = 12.5^\circ$, 19.1° , 20.0° , 22.3° , 23.0° , and 24.0° (Figure S6). These peaks are present in the PXRD pattern of desolvated HOF-GS-10, but desolvated HOF-GS-10 was not confirmed as guest-free by SCXRD. In fact, the SCXRD data herein demonstrates that the crystal structure of $(G)_2(1,5\text{-NDS})$ is markedly different upon ethanol removal (Figure S7, Table S2).

Figures 4c and 4d display the crystal structures of $(G)_2(1,5\text{-NDS})\text{EtOH}$ and $(G)_2(1,5\text{-NDS})$, respectively. The crystal density before and after ethanol removal remained unchanged at 1.44 g/cm^3 , indicating that the transformation was accompanied by a contraction of the crystal unit cell. This contraction primarily occurred through (i) a decrease in interlayer sheet spacing from 3.074 \AA to 2.772 \AA , (ii) distortion of the quasi-hexagonal arrangement of guanidinium and sulfonate ions, and (iii) rotation of the naphthalene pillars (Figure 4c-f, Figures S8-9). The herringbone packing arrangement of naphthalene molecules with orthogonal polarizabilities of $(G)_2(1,5\text{-NDS})$ likely results in the low retardance observed in Figure 4b.

As displayed by the green dashed circle in Figure 4f, zero-dimensional (0-D) pores – empty, molecule-sized void spaces ($>25 \text{ \AA}^3$) that exhibit no discernible pore connectivity – are present in guest-free $(G)_2(1,5\text{-NDS})$. The molecular volume of ethanol is 67.5 \AA^3 . Using a probe radius of 1.2 \AA (the approximate size of a helium atom), the pore volume of $(G)_2(1,5\text{-NDS})$ was calculated to be 90.82 \AA^3 , corresponding to 9.7% of the unit cell volume (Figure S10). This pore volume is smaller than the 101.95 \AA^3 cavity occupied by ethanol (green filled circles in Figure 4e) prior to guest removal, consistent with framework contraction to form guest-free $(G)_2(1,5\text{-NDS})$. Isolated, 0-D cavities have not yet been reported in guest-free GS frameworks, although one-dimensional (1-D) and two-

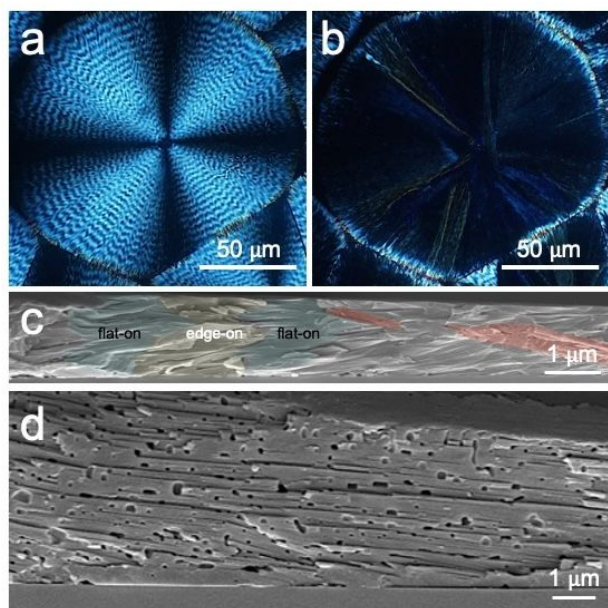


Figure 5. (a, b) Optical micrograph of a $(G)_2(1,5\text{-NDS})\supset\text{EtOH}$ banded spherulite viewed between crossed polarizers before and after ethanol removal, respectively. (c) Cross-sectional SEM image of a partially transformed $(G)_2(1,5\text{-NDS})\supset\text{EtOH}$ film collected parallel to the spherulite growth direction. Flat-on and edge-on oriented fibers are false-coloured blue and yellow, respectively, and a guest-free fiber is false-coloured red in (c). (d) Magnified region of a cross-sectional SEM image showing holes in the crystal fibers.

dimensional (2-D) cavities have been observed.^{44, 55} Crystallization of guest-free ethane-1,2-disulfonate from methanol, for example, affords bilayer galleries in which planar GS sheets are separated by the disulfonate pillars, which define 1-D channels.⁴⁴ On the other hand, bis(guanidinium) 1,4-benzenedisulfonate or $(G)_2(1,4\text{-BDS})\supset\text{acetone}$ is converted to $p\text{-}(G)_2(1,4\text{-BDS})$ upon removal of acetone guest and retains a continuous 2-D pore network wherein benzene rings can reorient, allowing for adsorption of nitrogen, carbon dioxide and xenon gases.⁵⁵ 0-D pores also have been reported in other molecular crystalline solids and have gained interest for their applications in rare gas sorption/desorption and storage.⁵⁷⁻⁶² The guest-free form of (\pm)-cryptophane-111 and its derivatives, for example, exhibit intrinsic cavities that can retain xenon gas at temperatures of up to 300°C.⁵⁹ To date, $(G)_2(1,5\text{-NDS})$ is the first demonstration of 0-D pores in guest-free GS frameworks. These void spaces in $(G)_2(1,5\text{-NDS})$ suggest prospects for gas absorption.

Guest removal from $(G)_2(1,5\text{-NDS})\supset\text{EtOH}$ banded spherulite films

A $(G)_2(1,5\text{-NDS})\supset\text{EtOH}$ banded spherulite film was heated at 130°C overnight using the same procedure as for single crystals. Figures 5a and 5b display optical micrographs of the film viewed between crossed polarizers before and after heating, respectively. Guest-free crystals nucleated on the surface of $(G)_2(1,5\text{-NDS})\supset\text{EtOH}$ banded spherulites from which their crystallization commenced to produce a guest-free film with

loss of banding (Video S2). Like the guest-free single crystal, the desolvated crystals in the film lost their interference colors between crossed polarizers which indicate a significant decrease in linear retardance compared to the banded spherulites. This finding is supported by $|LR|$ and LR_{angle} maps before and after ethanol removal (Figure S11) which show a decrease in linear retardance of the spherulite from 2.3-2.9 radians before ethanol removal to 0.3-0.5 radians after ethanol removal. The PXRD pattern obtained for the guest-free film matched the simulated PXRD pattern of the guest-free single crystals (Figure S6), indicating that ethanol was removed from the crystals in the film. Further, the PXRD pattern for the desolvated bulk powder matched the simulated PXRD pattern of guest-free $(G)_2(1,5\text{-NDS})$ (Figure S6).

Cross-sectional SEMs of a partially transformed $(G)_2(1,5\text{-NDS})\supset\text{EtOH}$ banded spherulite film at different magnifications collected along the spherulite growth direction, are displayed in Figures 5c and 5d. Platelike crystals with holes (false-colored red in Figure 5c) grew diagonally through flat-on (false-colored blue in Figure 5c) and edge-on (false-colored yellow in Figure 5c) regions of the banded spherulite towards the substrate surface. As the film was heated, ethanol was released at the film surface, and the film became visibly smoother. Cracks and holes developed in the crystal fibers. Closer examination of the guest-free crystals in the cross-section in Figure 5d revealed stacked crystallites, with holes less than 1 μm in diameter. The SEM cross-section of the guest-free crystals were further analyzed using the thresholding tool in Fiji software (Figure S12). Analysis of 142 pores revealed that they were circular and convex, with an average pore area of 5 nm^2 and individual pore areas ranging from 0.27 nm^2 to 37 nm^2 .

Conclusions

Significant strides have been made in the development and synthesis of functional hydrogen-bonded frameworks. A number of these materials have been inherently chiral, primarily due to the incorporation of chiral pillars in their construction. Herein, we have introduced mesoscale chirality to $(G)_2(1,5\text{-NDS})\supset\text{EtOH}$ films through crystal twisting rendering them optically active, albeit at the mesoscale. Subsequent guest removal resulted in a loss of optical activity. The modular nature of twisted GS frameworks promises a strategy to interrogate crystal orientation-dependent properties while modulating the chiroptical response. The demonstration of 0-D porosity in guest-free $(G)_2(1,5\text{-NDS})$ further emphasizes the potential for GS frameworks to be used for separation and gas storage applications.

Materials and methods

Materials

$(G)_2(1,5\text{-NDS})$ was synthesized according to previously published procedures.⁴⁸ Alcohol 200 proof, methanol, acetone, and water were purchased from Pharmco by Greenfield Global (Brookfield, CT) and used without further purification.

Guanidinium tetrafluoroborate, disodium naphthalene-1,5-disulfonate salt, and other materials were purchased from Sigma-Aldrich (St. Louis, MO). Glass cover-slips were pre-cleaned by performing three 15-minute washes with water, acetone, then ethanol. The glass cover-slips were then dried in an oven at 80°C for 5 minutes, followed by a 10-minute treatment with uv/ozone. (G)₂(1,5-NDS) solutions were prepared by mixing (G)₂(1,5-NDS) in ethanol at a concentration of 10 mg/mL concentration. The mixture was sonicated for 1 minute, then heated with stirring at 50°C. This sample was diluted to obtain solutions with concentrations of 5.0, 2.0, 1.0, 0.50, 0.25 and 0.10 mg/mL at 50°C. (G)₂(1,5-NDS)⊃EtOH films were fabricated by drop casting 30 μL of hot (G)₂(1,5-NDS) ethanol solution onto pre-cleaned glass coverslips stored uncovered at -78, 0, 25, 40, 50 and 60°C in a ventilated hood for 1 minute to 1 hour depending on the substrate temperature. (G)₂(1,5-NDS)⊃EtOH banded spherulite films were placed in an oven overnight at 130°C, affording guest-free (G)₂(1,5-NDS) films.

Optical characterization

Optical micrographs between crossed polarizers were collected with an Olympus BX53 microscope. Mueller matrix images were collected on a home-built instrument equipped with a FLIR Blackfly BFS-U3-5155P-C camera, in accordance with previously published designs.⁴⁹

Powder X-ray diffraction

2-D XRD patterns were collected on (G)₂(1,5-NDS) films with a Bruker D8 Discover General Area Detector Diffraction System (GADDS) equipped with a VÅNTEC-2000 2-D detector and Cu-K α source (λ = 1.54178 Å). The X-ray beam was monochromated with a graphite crystal and collimated with a 0.50 mm capillary collimator (MONOCAP).

Crystal growth

Bulk powders of (G)₂(1,5-NDS)⊃EtOH were obtained by recrystallization from ethanol in an ice-water bath. Single crystals of (G)₂(1,5-NDS)⊃EtOH were obtained by evaporation of ethanol containing GS apohost (1 mg in 1 mL of ethanol). Crystallization was performed in a 20 mL scintillation vial. Single crystals were typically achieved by slow evaporation of the solvent under ambient temperature over a period of 1 to 7 days. Bulk powders and single crystals of (G)₂(1,5-NDS)⊃EtOH with hexagonal, colorless plate habit were placed in an oven overnight at 130°C, affording guest-free (G)₂(1,5-NDS).

Single-crystal X-ray diffraction

Single-crystal X-ray diffraction data was obtained using a Bruker SMART APEX II diffractometer equipped with a PHOTON-II-C14 detector. The X-ray beam generated from an INCOATEC micro-focused Mo source (λ = 0.71073 Å) was monochromated and collimated by a Montel multilayer optics. Crystal temperature was controlled by an Oxford Cryosystems 700+ Cooler. The crystal was mounted on a 0.2 mm MiTeGen MicroMount with

Type B immersion oil (Cargille Labs). A phi scan (APEX4) was performed to evaluate the crystal quality and determine the data collection parameters. Full datasets were collected with omega scan methods. The data sets were processed with the INTEGRATE program of the APEX4 software for reduction and cell refinement.⁶³ Multi-scan absorption corrections were applied by the SCALE program for the area detector. Two structures were solved by intrinsic phasing methods (SHELXT) and the structure models were completed and refined using the full-matrix least-square methods on *F*² (SHELXL).⁶⁴ Non-hydrogen atoms in the structures were refined with anisotropic displacement parameters, and hydrogen atoms on the carbons were placed in idealized positions (C-H = 0.95 - 1.00 Å) and included as riding with *U*_{iso(H)} = 1.2 or 1.5 *U*_{eq(non-H)}.

Scanning electron microscopy

After crystallization, a 2 nm-thick platinum coating was deposited on the surface of the film using a Cressington 208HR Sputter Coater equipped with a MTM-20 thickness controller. Films were then cut at the desired cross-section and both the film surface, and the cross-section were imaged. Top-view and cross-sectional scanning electron micrographs were collected with a Merlin Field-Emission Scanning Electron Microscope (Carl Zeiss) with an electron high tension voltage of 4.00 kV.

Author contributions

R. B. S.: investigation, data curation, formal analysis, methodology, and writing - original draft. A. Y.: investigation, methodology, formal analysis. A. M. D.: investigation, methodology, resources, formal analysis and writing - review and editing. O. O.: methodology. S. S.: formal analysis. A. T. and S. J. W.: investigation. W. W.: investigation. Z. C.: validation. A. G. S.: formal analysis and writing - review and editing. M. D. W., B. K. and S. S. L.: writing - review and editing, supervision and funding acquisition.

Conflicts of interest

There are no conflicts to declare.

Data availability

The data supporting this article have been included as part of the ESI. Crystallographic data for (G)₂(1,5-NDS)⊃EtOH, including cif, res, fcf, and hkl files, have been deposited at the Cambridge Crystallographic Data Centre under CCDC deposition number 2419508. Copies of these data can be requested, free of charge, from the CCDC website at <https://www.ccdc.cam.ac.uk/structures/>.

Acknowledgements

We thank Professor K. Travis Holman for helpful discussions on porous hydrogen-bonded frameworks. We acknowledge support from the National Science Foundation (NSF) through

awards DMR-2116183, DMR-2002964, and CMMI-2325911 and the New York University Materials Research Science and Engineering Center (MRSEC) program of the NSF under award number DMR-1420073. The GADDS microdiffractometer was acquired through the support of the NSF under award number CRIF/CHE-0840277 and NSF MRSEC Program under award number DMR-0820341. We also acknowledge support from the Margaret and Herman Sokol Fellowship.

References

1. A. M. Dillon, A. Yusov, M. T. Chaudhry, J. A. Newman, K. M. Demkiw, K. A. Woerpel, A. Y. Lee and M. D. Ward, *Crystal Growth & Design*, 2024, **24**, 3483-3490.
2. V. A. Russell, M. C. Etter and M. D. Ward, *Journal of the American Chemical Society*, 1994, **116**, 1941-1952.
3. M. J. Horner, K. T. Holman and M. D. Ward, *Journal of the American Chemical Society*, 2007, **129**, 14640-14660.
4. M. J. Horner, K. T. Holman and M. D. Ward, *Angewandte Chemie International Edition*, 2001, **40**, 4045-4048.
5. K. T. Holman, A. M. Pivovar, J. A. Swift and M. D. Ward, *Accounts of Chemical Research*, 2001, **34**, 107-118.
6. A. Comotti, S. Bracco, P. Sozzani, S. M. Hawxwell, C. Hu and M. D. Ward, *Crystal Growth & Design*, 2009, **9**, 2999-3002.
7. Y. Liu, W. Xiao, J. J. Yi, C. Hu, S.-J. Park and M. D. Ward, *Journal of the American Chemical Society*, 2015, **137**, 3386-3392.
8. A. G. Shtukenberg, X. Zhu, Y. Yang and B. Kahr, *Crystal Growth & Design*, 2020, **20**, 6186-6197.
9. Y. Yang, Y. Zhang, C. T. Hu, M. Sun, S. Jeong, S. S. Lee, A. G. Shtukenberg and B. Kahr, *Chemistry of Materials*, 2022, **34**, 1778-1788.
10. S. Jeong, N. Barbosa, A. Tiwari, E. K. Holland, L.-Y. Huang, V. Bhat, Y. Yang, Y. Zhang, S. J. Whittaker, M.-W. Kim, A. Alaei, P. Sundaram, R. Spencer, J. Brazard, D. M. Kalyon, C. Risko, J. E. Anthony, T. B. M. Adachi, A. G. Shtukenberg, ... and S. S. Lee, *Advanced Functional Materials*, 2023, **33**, 2212531.
11. I. Lozano, S. J. Whittaker, Y. Yang, A. Tiwari, H. Zhou, S. Kim, M. Mendoza, M. Sow, A. G. Shtukenberg, B. Kahr, Z. An and S. S. Lee, *Chirality*, 2023, **35**, 418-426.
12. Y. Yang, L. Silva de Moraes, C. Ruzié, G. Schweicher, Y. H. Geerts, A. R. Kennedy, H. Zhou, S. J. Whittaker, S. S. Lee, B. Kahr and A. G. Shtukenberg, *Advanced Materials*, 2022, **34**, 2203842.
13. Y. Yang, K. Zong, S. J. Whittaker, Z. An, M. Tan, H. Zhou, A. G. Shtukenberg, B. Kahr and S. S. Lee, *Molecular Systems Design & Engineering*, 2022, **7**, 569-576.
14. B. Kahr, Y. Yang, S. J. Whittaker, A. G. Shtukenberg and S. Lee, *Helvetica Chimica Acta*, 2023, **106**, e202200202.
15. S. J. Whittaker, H. Zhou, R. B. Spencer, Y. Yang, A. Tiwari, J. Bendesky, M. McDowell, P. Sundaram, I. Lozano, S. Kim, Z. An, A. G. Shtukenberg, B. Kahr and S. S. Lee, *Crystal Growth & Design*, 2024, **24**, 613-626.
16. T. Adachi, D. M. Connors, W. Xiao, C. Hu and M. D. Ward, *Crystal Growth & Design*, 2015, **15**, 3366-3373.
17. A. C. Soegiarto and M. D. Ward, *Crystal Growth & Design*, 2009, **9**, 3803-3815.
18. A. Yusov, A. M. Dillon, C. T. Hu, S. S. Lee and M. D. Ward, *Organic Electronics*, 2023, **115**, 106752.
19. A. C. Soegiarto, A. Comotti and M. D. Ward, *Journal of the American Chemical Society*, 2010, **132**, 14603-14616.
20. M. Rohullah, V. V. Pradeep, J. Ravi, A. V. Kumar and R. Chandrasekar, *Angewandte Chemie International Edition*, 2022, **61**, e202202114.
21. A. G. Shtukenberg, Y. O. Punin, A. Gujral and B. Kahr, *Angewandte Chemie International Edition*, 2014, **53**, 672-699.
22. A. G. Shtukenberg, R. Drori, E. V. Sturm, N. Vidavsky, A. Haddad, J. Zheng, L. A. Estroff, H. Weissman, S. G. Wolf, E. Shimoni, C. Li, N. Fellah, E. Efrati and B. Kahr, *Angewandte Chemie International Edition*, 2020, **59**, 14593-14601.
23. E. M. Woo, G. Lugito and C.-E. Yang, *CrystEngComm*, 2016, **18**, 977-985.
24. E. Gunn, *Small molecule banded spherulites*, University of Washington, 2009.
25. A. G. Shtukenberg, A. Gujral, E. Rosseeva, X. Cui and B. Kahr, *CrystEngComm*, 2015, **17**, 8817-8824.
26. S. J. Whittaker, M. McDowell, J. Bendesky, Z. An, Y. Yang, H. Zhou, Y. Zhang, A. G. Shtukenberg, D. M. Kalyon, B. Kahr and S. S. Lee, *Chemistry of Materials*, 2023, **35**, 8599-8606.
27. X. Cui, A. L. Rohl, A. Shtukenberg and B. Kahr, *Journal of the American Chemical Society*, 2013, **135**, 3395-3398.
28. A. T. Martin, S. M. Nichols, V. L. Murphy and B. Kahr, *Chemical Communications*, 2021, **57**, 8107-8120.
29. R. D. Deegan, O. Bakajin, T. F. Dupont, G. Huber, S. R. Nagel and T. A. Witten, *Nature*, 1997, **389**, 827-829.
30. R. D. Deegan, O. Bakajin, T. F. Dupont, G. Huber, S. R. Nagel and T. A. Witten, *Physical Review E*, 2000, **62**, 756-765.
31. H. Hu and R. G. Larson, *The Journal of Physical Chemistry B*, 2002, **106**, 1334-1344.
32. L. Gránásy, T. Pusztai, G. Tegze, J. A. Warren and J. F. Douglas, *Physical Review E*, 2005, **72**, 011605.
33. A. G. Shtukenberg, Y. O. Punin, E. Gunn and B. Kahr, *Chemical Reviews*, 2012, **112**, 1805-1838.
34. J.-i. Suda, T. Nakayama, A. Nakahara and M. Matsushita, *Journal of the Physical Society of Japan*, 1996, **65**, 771-777.
35. S. Ibe, R. Ise, Y. Oaki and H. Imai, *CrystEngComm*, 2012, **14**, 7444-7449.
36. X. Cui, A. G. Shtukenberg, J. Freudenthal, S. Nichols and B. Kahr, *Journal of the American Chemical Society*, 2014, **136**, 5481-5490.
37. A. Shtukenberg, E. Gunn, M. Gazzano, J. Freudenthal, E. Camp, R. Sours, E. Rosseeva and B. Kahr, *ChemPhysChem*, 2011, **12**, 1558-1571.
38. E. Gunn, R. Sours, J. B. Benedict, W. Kaminsky and B. Kahr, *J Am Chem Soc*, 2006, **128**, 14234-14235.
39. Y. Yang, A. G. Shtukenberg, H. Zhou, C. Ruzie, Y. H. Geerts, S. S. Lee and B. Kahr, *Chemistry of Materials*, 2024, **36**, 881-891.
40. T. Adachi and M. D. Ward, *Accounts of Chemical Research*, 2016, **49**, 2669-2679.
41. C. C. Evans, L. Sukarto and M. D. Ward, *Journal of the American Chemical Society*, 1999, **121**, 320-325.
42. A. Yusov, A. M. Dillon and M. D. Ward, *Molecular Systems Design & Engineering*, 2021, **6**, 756-778.
43. A. Yusov, A. M. Dillon, M. T. Chaudhry, J. A. Newman, A. Y. Lee and M. D. Ward, *ACS Materials Letters*, 2024, **6**, 1906-1912.
44. V. A. Russell, C. C. Evans, W. Li and M. D. Ward, *Science*, 1997, **276**, 575-579.

45. A. M. Dillon, A. G. Shtukenberg, K. M. Demkiw, K. A. Woerpel and M. D. Ward, *Chemical Communications*, 2024, **60**, 11770-11773.
46. N. J. Burke, A. D. Burrows, M. F. Mahon and J. E. Warren, *CrystEngComm*, 2008, **10**, 15-18.
47. C. Shi, B. Wei and W. Zhang, *Crystal Growth & Design*, 2014, **14**, 6570-6580.
48. Y. Li, S. Tang, A. Yusov, J. Rose, A. N. Borrfors, C. T. Hu and M. D. Ward, *Nature Communications*, 2019, **10**, 4477.
49. D. Gottlieb and O. Arteaga, *Optics Express*, 2021, **29**, 34723-34734.
50. O. Arteaga and R. Ossikovski, *Journal of the Optical Society of America A*, 2019, **36**, 416-427.
51. A. G. Shtukenberg, X. Cui, J. Freudenthal, E. Gunn, E. Camp and B. Kahr, *Journal of the American Chemical Society*, 2012, **134**, 6354-6364.
52. Y. Li, M. Handke, Y.-S. Chen, A. G. Shtukenberg, C. T. Hu and M. D. Ward, *Journal of the American Chemical Society*, 2018, **140**, 12915-12921.
53. W. Xiao, C. Hu and M. D. Ward, *Journal of the American Chemical Society*, 2014, **136**, 14200-14206.
54. Y. Liu and M. D. Ward, *Crystal Growth & Design*, 2009, **9**, 3859-3861.
55. I. Brekalo, D. E. Deliz, L. J. Barbour, M. D. Ward, T. Friščić and K. T. Holman, *Angewandte Chemie International Edition*, 2020, **59**, 1997-2002.
56. A. Karmakar, R. Illathvalappil, B. Anothumakkool, A. Sen, P. Samanta, A. V. Desai, S. Kurungot and S. K. Ghosh, *Angewandte Chemie*, 2016, **128**, 10825-10829.
57. P. K. Thallapally, G. O. Lloyd, J. L. Atwood and L. J. Barbour, *Angewandte Chemie International Edition*, 2005, **44**, 3848-3851.
58. C. M. Kane, A. Banisafar, T. P. Dougherty, L. J. Barbour and K. T. Holman, *Journal of the American Chemical Society*, 2016, **138**, 4377-4392.
59. A. I. Joseph, S. H. Lapidus, C. M. Kane and K. T. Holman, *Angewandte Chemie International Edition*, 2015, **54**, 1471-1475.
60. L. J. Barbour, *Chemical Communications*, 2006, 1163-1168.
61. J. L. Atwood, L. J. Barbour, A. Jerga and B. L. Schottel, *Science*, 2002, **298**, 1000-1002.
62. C. M. Kane, O. Ugono, L. J. Barbour and K. T. Holman, *Chemistry of Materials*, 2015, **27**, 7337-7354.
63. *Journal*, 2020.
64. G. Sheldrick, *Acta Crystallographica Section A*, 2015, **71**, 3-8.

Data availability

The data supporting this article have been included as part of the ESI. Crystallographic data for (G)₂(1,5-NDS)⊃EtOH, including cif, res, fcf, and hkl files, have been deposited at the Cambridge Crystallographic Data Centre under CCDC deposition number 2419508. Copies of these data can be requested, free of charge, from the CCDC website at <https://www.ccdc.cam.ac.uk/structures/>.